Bio-Design and Manufacturing (2024) 7:439–452
https://doi.org/10.1007/s42242-023-00266-y

RESEARCH ARTICLE

Deep brain implantable microelectrode arrays for detection and functional localization of the subthalamic nucleus in rats with Parkinson's disease

Luyi Jing[1,2] · Zhaojie Xu[1,2] · Penghui Fan[1,2] · Botao Lu[1,2] · Fan Mo[1,2] · Ruilin Hu[1,2] · Wei Xu[1,2] · Jin Shan[1,2] · Qianli Jia[1,2] · Yuxin Zhu[1,2] · Yiming Duan[1,2] · Mixia Wang[1,2] · Yirong Wu[1,2] · Xinxia Cai[1,2]

Received: 14 June 2023 / Accepted: 17 December 2023 / Published online: 22 February 2024

Abstract

The subthalamic nucleus (STN) is considered the best target for deep brain stimulation treatments of Parkinson's disease (PD). It is difficult to localize the STN due to its small size and deep location. Multichannel microelectrode arrays (MEAs) can rapidly and precisely locate the STN, which is important for precise stimulation. In this paper, 16-channel MEAs modified with multiwalled carbon nanotube/poly(3,4-ethylenedioxythiophene):poly(styrene sulfonate) (MWCNT/PEDOT:PSS) nanocomposites were designed and fabricated, and the accurate and rapid identification of the STN in PD rats was performed using detection sites distributed at different brain depths. These results showed that nuclei in 6-hydroxydopamine hydrobromide (6-OHDA)-lesioned brains discharged more intensely than those in unlesioned brains. In addition, the MEA simultaneously acquired neural signals from both the STN and the upper or lower boundary nuclei of the STN. Moreover, higher values of spike firing rate, spike amplitude, local field potential (LFP) power, and beta oscillations were detected in the STN of the 6-OHDA-lesioned brain, and may therefore be biomarkers of STN localization. Compared with the STNs of unlesioned brains, the power spectral density of spikes and LFPs synchronously decreased in the delta band and increased in the beta band of 6-OHDA-lesioned brains. This may be a cause of sleep and motor disorders associated with PD. Overall, this work describes a new cellular-level localization and detection method and provides a tool for future studies of deep brain nuclei.

✉ Mixia Wang
wangmixia@mail.ie.ac.cn

✉ Yirong Wu
wyr@mail.ie.ac.cn

✉ Xinxia Cai
xxcai@mail.ie.ac.cn

[1] State Key Laboratory of Transducer Technology, Aerospace Information Research Institute, Chinese Academy of Sciences, Beijing 100190, China

[2] School of Electronic, Electrical and Communication Engineering, University of Chinese Academy of Sciences, Beijing 100049, China

Graphic abstract

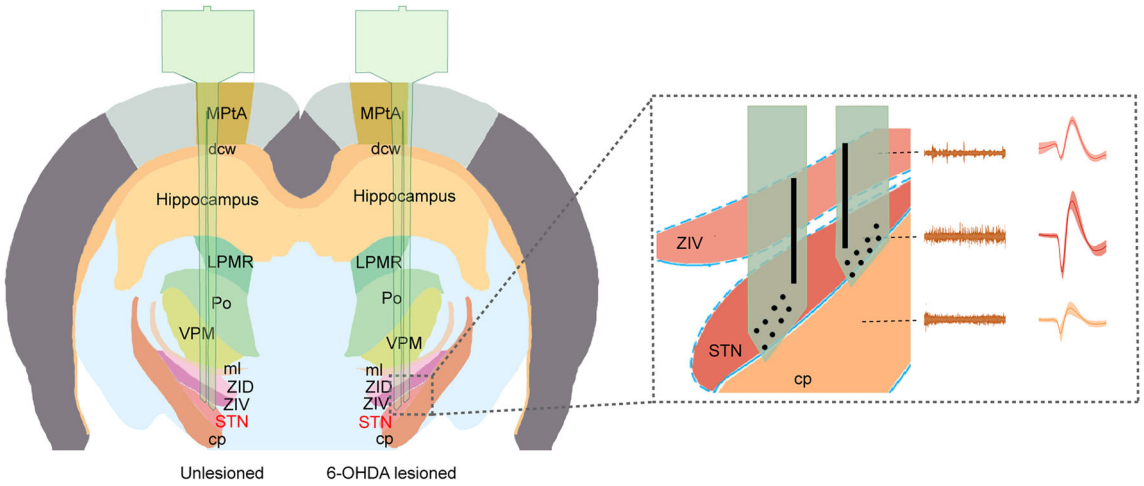

Keywords Functional localization · Implantable microelectrode arrays · Parkinson's disease · Subthalamic nucleus

Introduction

Parkinson's disease (PD) is a serious disorder that occurs mainly in elderly individuals and affects tens of millions of people worldwide [1, 2]. In the past, levodopa was considered the best treatment for PD, but this treatment causes serious complications for patients [3, 4]. Compared to medication, deep brain stimulation (DBS) has demonstrated significant advantages for reducing these complications [5]. The subthalamic nucleus (STN) has been considered the best target for DBS since its stimulation confers greater therapeutic effects and is associated with fewer complications [6]. However, precise targeting of the STN is crucial for effective treatment [7, 8].

Current medical imaging technologies cannot accurately identify the STN due to its small size and deep location. For example, the clinical accuracy of existing intraoperative stereotactic systems is 0.1–0.5 mm, which is close to the size of the STN itself (which has a short diameter of 4–6 mm and a long diameter of 10–12 mm) [9]. Therefore, detection electrodes are often used to assist in the precise localization of the STN so that stimulation electrodes can access the optimal target site [10, 11]. Previously described techniques for detection of the STN have mainly used tungsten-tipped microelectrodes [12] or semimicroelectrodes [13, 14]. The spatial resolution of the neural information obtained by semimicroelectrodes is low and cannot specifically identify individual neurons [15]. Moreover, tungsten-tipped microelectrodes cannot simultaneously identify electrophysiological characteristics at different depths due to their low number of channels; this reduces the efficiency and accuracy of localization. Thus, there is an urgent need to design and fabricate multichannel microelectrode arrays (MEAs) that can rapidly and precisely recognize the STN via cellular-level detection without requiring the implantation of multiple neural microprobes.

Specific firing patterns and beta (13–30 Hz) oscillatory activities are characteristic features of the STN found in Parkinsonian patients [16, 17]. However, to date studies of PD treatments have obtained less neural information regarding the STN on the cellular level. The size of the detection sites of implantable MEAs matches the size of individual neurons, and they can therefore acquire neural information on the single-cell level [18–20]. In addition, implantable MEAs can make use of multiple small detection sites to improve spatial resolution. Given these advantages, the development of MEAs has significantly boosted research on the mechanistic basis of PD treatments [21, 22]. Obtaining additional neural information regarding the STN may contribute to more precise localization and provides a basis for effective treatment of PD.

Conductive polymers are commonly used to modify neural microelectrodes to enhance their electrical performance [23]. Poly(3,4-ethylenedioxythiophene) (PEDOT) is a widely used conductive polymer, since it possesses excellent biocompatibility and environmental stability [24, 25]. In a recent paper, Ludwig et al. showed that silicon microelectrodes modified with PEDOT films can still obtain high-quality neural recordings within six weeks [26]. However, since pure PEDOT has poor processability, it is generally blended with poly(styrene sulfonate) (PSS) and other macromolecular dopants to form PEDOT:PSS composites, which improve its performance. This is because PEDOT:PSS composites retain the conductivity of PEDOT but have better

solubility and film-forming properties [27, 28]. Furthermore, PEDOT:PSS has good biocompatibility, which can reduce the incidence of negative brain tissue reactions and promote the growth of neurons [29]. Carbon nanotubes (CNTs) can reduce electrode impedance and enhance charge transfer, thereby improving neural signal detection [30, 31]. They have therefore been considered one of the most promising materials for neural microelectrodes in recent years [32]. A combination of PEDOT and multiwalled carbon nanotubes (MWCNTs) can promote cell adhesion and neurite outgrowth. For example, compared to bare platinum electrodes, electrodes modified with PEDOT/MWCNTs have been found to induce less severe tissue reactions [30]. Therefore, in this paper, we used a MWCNTs/PEDOT:PSS treatment framework to improve MEA performance.

In this study, the described MEAs were designed and fabricated using a microelectromechanical system (MEMS). The detection sites of the MEA were distributed at different depths such that the novel MEA could simultaneously acquire neural signals from the STN and its upper (or lower) boundary nuclei. Furthermore, MEA detection sites were designed to fit the shape of the STN, and these sites were closely aligned, which allowed for a greater quantity of neural information at the cellular level to be captured, thereby facilitating accurate and rapid localization of the STN. Neural information of nuclei in unlesioned brains was also obtained as a negative control. In summary, we found that the MEA system described here was highly efficient for the localization and detection of deep brain nuclei.

Materials and methods

Design of a deep brain implantable MEA

First, a two-shank (16-channel) MEA was designed and fabricated for functional localization and detection of the STN (Fig. 1a). As shown in Fig. 1b, the electrode tips were

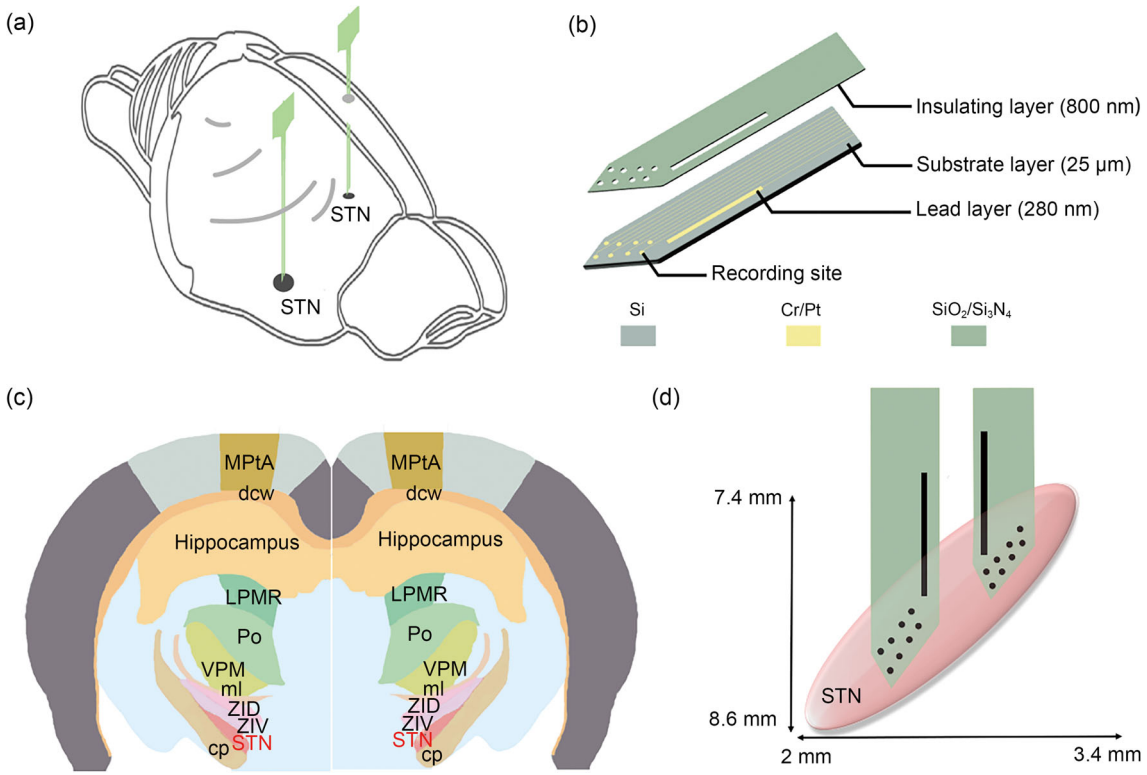

Fig. 1 Schematic diagram of MEA implantation. **a** Two MEAs were simultaneously implanted into the bilateral brain to localize and detect the STN. **b** Three layers of the MEA: the lead layer, the substrate layer, and the insulating layer. **c** Brain mapping of MEA pathway nuclei during implantation. **d** MEA sites were designed to fit the shape of the STN. MEA: microelectrode array; STN: subthalamic nucleus; MPtA: medial parietal association cortex; dcw: deep cerebral white matter; LPMR: lateral posterior thalamic nucleus, mediorostral part; Po: the post thalamic nuclear group; VPM: the ventral posteromedial thalamic nucleus; ml: medial lemniscus; ZID: the dorsal part of the zona incerta; ZIV: the ventral part of the zona incerta; cp: cerebral peduncle

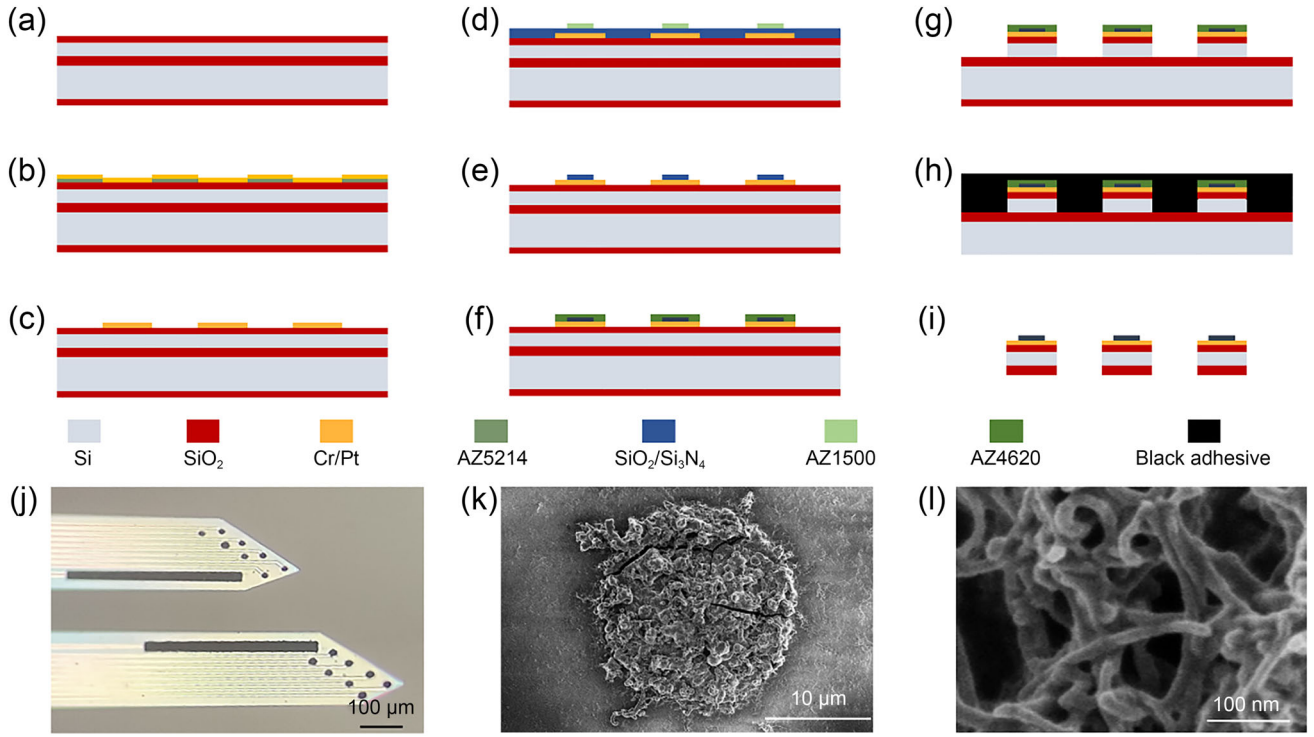

Fig. 2 Schematic diagram of the MEA. **a** SiO_2 was deposited on the SOI surface via thermal oxidation. **b** Deposition of Cr/Pt and spin coating of AZ5214. **c** Lift-off of Cr/Pt to form the conductive layer. **d** Deposition of the insulating layer SiO_2/Si_3N_4 and patterning by AZ1500. **e** Etching the insulating layer using CHF_3 ion etching to expose the electrode. **f** Spin coating and patterning by AZ4620. **g** Etching the shape layer via deep etching. **h** Etching SiO_2 on the backside of the SOI and protecting the front electrode using black adhesive. **i** Release of the electrode by KOH wet etching. **j** Micrograph of the MEA. **k**, **l** SEM images of MEA sites. MEA: microelectrode array; SOI: silicon-on-insulator; SEM: scanning electron microscopy

designed to be sharp-angled, which can facilitate implantation and reduce damage to the brain tissue. The detection sites of the MEA were distributed at different depths so that the MEA could simultaneously detect nuclei present at any depth. Each probe was 150 μm×25 μm (width×thickness) in cross-section and was separated by 90 μm. Each probe was 9.5 mm in length, and could obtain electrophysiological signals from the medial parietal association cortex (MPtA) to the STN as well as across the STN, as shown in Fig. 1c. As shown in Fig. 1d, each probe contained 16 recording sites (diameter=10 μm), a counter site (20 μm×300 μm), and a reference site (20 μm×300 μm). The small diameter of the detection sites enables neural signal detection on the single-cell level. Furthermore, the dimensional parameters of the MEA were selected to match the anatomy of the STN, which has a maximum width of 400 μm in the coronal plane, a depth ranging from 7.4 to 8.6 mm, and an incline of 45°. In this study, which used a rat model system, the detection sites of the MEA were designed to fit the specific STN shape of rats (Fig. 1d). Moreover, sites were closely aligned to allow for more neural information on the cellular level to enable accurate and precise localization of the STN. Figure S1 (Supplementary Information) shows how MEAs were implanted according to their expected path and localized to the STN. Brain slice analysis showed that the electrode was restricted within the target nucleus during longitudinal implantation, and did not damage surrounding nuclei.

Fabrication of a deep brain implantable MEA

As a material, silicon possesses good biocompatibility and toughness, and it is therefore suitable for the localization and detection of deep brain nuclei. In this paper, we chose silicon to be the substrate of the MEA, which was then fabricated by MEMS. As shown in Fig. 1b, the fabricated MEA contains three layers: a substrate layer (25 μm thick), a lead layer (280 nm thick), and an insulating layer (800 nm thick). The layered MEA was patterned onto a silicon-on-insulator (SOI) device. The detailed manufacturing process is as follows. Initially, SiO_2 was deposited on the SOI surface by thermal oxidation (Fig. 2a). Next, the conducting layer was formed by photolithography, the deposition of Cr/Pt (Fig. 2b), and a subsequent lift-off (Fig. 2c). Thereafter, SiO_2/Si_3N_4 was deposited to establish the insulator area and patterned using a second photolithography process (Fig. 2d). Next, all bonding pads, recording sites, the counter site, and the reference site

were exposed by CHF_3 ion etching (Fig. 2e). The shape of the MEA was then selectively deep etched using the third mask plate (Figs. 2f and 2g). Finally, after etching SiO_2 onto the back side of the electrode (Fig. 2h), individual electrodes were released by corrosion of the back side of the SOI using a high-temperature KOH solution (Fig. 2i). KOH does not easily react with SiO_2, and wet corrosion can automatically stop after completion due to the SiO_2 present on the bottom layer of the SOI.

Following that, MEAs were modified with MWCNTs/PEDOT:PSS to enhance their electrical properties. This modification process is shown in Fig. S2 (Supplementary Information). The mixing ratio of the nanomaterials used in this paper refers to a ratio previously proposed in the scientific literature [29, 33]. First, a 0.2 mol/L PSS (HEROCHEM, China) solution was added to a 4 mg/mL MWCNT preparation (XFNANO, China), and was subjected to an ultrasound treatment for 60 min. Next, 40 mmol/L 3,4-ethylenedioxythiophene (EDOT, Aladdin, China) was added to this dispersion, and the ultrasound was maintained until a homogeneous suspension was obtained. The EDOT monomer was then fully dissolved in PSS, since PSS can promote the dissolution of EDOT. Moreover, the MWCNTs were closely connected with EDOT:PSS due to π–π bond interactions. For optimal deposition, MEAs were cleaned using an oxygen-reactive ion etching procedure prior to modification. A three-electrode system was used for the process of MEA modification of the MWCNT/PEDOT:PSS nanocomposite material, in which Pt was used as the counter electrode and Ag/AgCl as the reference electrode. Cyclic voltammetry was used during the modification process, with scanning at 100 mV/s at 0–0.95 V for at least 20 cycles. During the electrodeposition process, EDOT underwent an oxidation reaction to form PEDOT. PEDOT then embedded MWCNTs into its long chain structure via a chemical coupling reaction and firmly immobilized them on the microelectrode surface. Finally, MWCNTs/PEDOT:PSS were firmly fixed on the metal surface of the electrode.

Preparation of a Parkinsonian rat model

Here, we first obtained 250–300 g male Wistar rats (Vital River, Beijing, China) to establish a Parkinsonian model system. All experimental rats were housed in a single cage, and the temperature ((22±2) °C) and humidity (40%±5%) of the living environment were in accordance with normal experimental animal feeding standards.

During experimentation, rats were fixed on a stereotaxic device (51,600, Stoelting, USA) using continuous anesthesia. A small craniotomy was made over the substantia nigra compacta (SNc; anterior–posterior: −4.9 mm; medial–lateral: 2.0 mm; dorsal–ventral: −8.2 mm) and medial forebrain bundle (MFB; anterior–posterior: −3.6 mm; medial–lateral: 1.8 mm; dorsal–ventral: −8.4 mm) of the right hemisphere of the rat brains. Next, 4 μL 6-hydroxydopamine hydrobromide (6-OHDA, ACMEC, China) (i.e., 8 μg 6-OHDA added to 4 μL 0.2% ascorbate (ACMEC, China) solution) was injected into the SNc and MFB areas separately (Fig. S3a in Supplementary Information). After surgery, the rats were subcutaneously injected with R-(-)-apomorphine (Aladdin, China) (0.1 mg/kg) to verify whether the Parkinsonian model transformation was effective; this occurred after at least 72 h of recovery (Fig. S3b in Supplementary Information). If the rat rotated toward its healthy side with an average speed greater than 7 r/min, the rat was considered a successful PD model (Video S1 in Supplementary Information).

Protocol for positioning and recording the brains of PD rats

PD rats (n=3) were fixed in a stereotaxic apparatus under anesthesia by RWD520 isoflurane (with the anesthetic concentration maintained at 1.5%). As shown in Fig. 1a, two craniotomies were performed to expose sites for the implantation of the two MEAs (anterior–posterior: −3.6 mm; medial–lateral: ±2.5 mm).

In this paper, MEAs were implanted into the surface cortex using a micropositioner at an implant speed of 1 μm/s (Model 2662, David Kopf Instruments, USA). During implantation, the MEA was stopped and recorded for 10 min at any position until it crossed the target nucleus, i.e., the STN. As shown in Fig. 1c, the nucleus of the pathway implanted by the MEA includes the MPtA, the deep cerebral white matter (dcw), the hippocampus, the lateral posterior thalamic nucleus, mediorostral part (LPMR), the post thalamic nuclear group (Po), the ventral posteromedial thalamic nucleus (VPM), the medial lemniscus (ml), the dorsal part of the zona incerta (ZID), the ventral part of the zona incerta (ZIV), the STN, and the cerebral peduncle (cp). Specifically, the biosensor detected the boundaries of the STN as well as the nuclei above and below the STN. Electrophysiological signals produced between the depth of 600 μm and 8600 μm were recorded using a homemade electrophysiological recording system [34]. All signal detection was performed at 37 °C so as to keep rat subjects at a comfortable temperature.

Electrophysiological analysis

Spike features were extracted using the T-distribution E-M algorithm and by a valley-seeking algorithm form of principal component analysis. Spike and local field potential (LFP) data were then analyzed by Neuroexplorer before being statistically processed and graphed using Origin 2018 (Origin Lab, USA). All summary data reported in this paper were computed as mean±standard error (SE). One-way

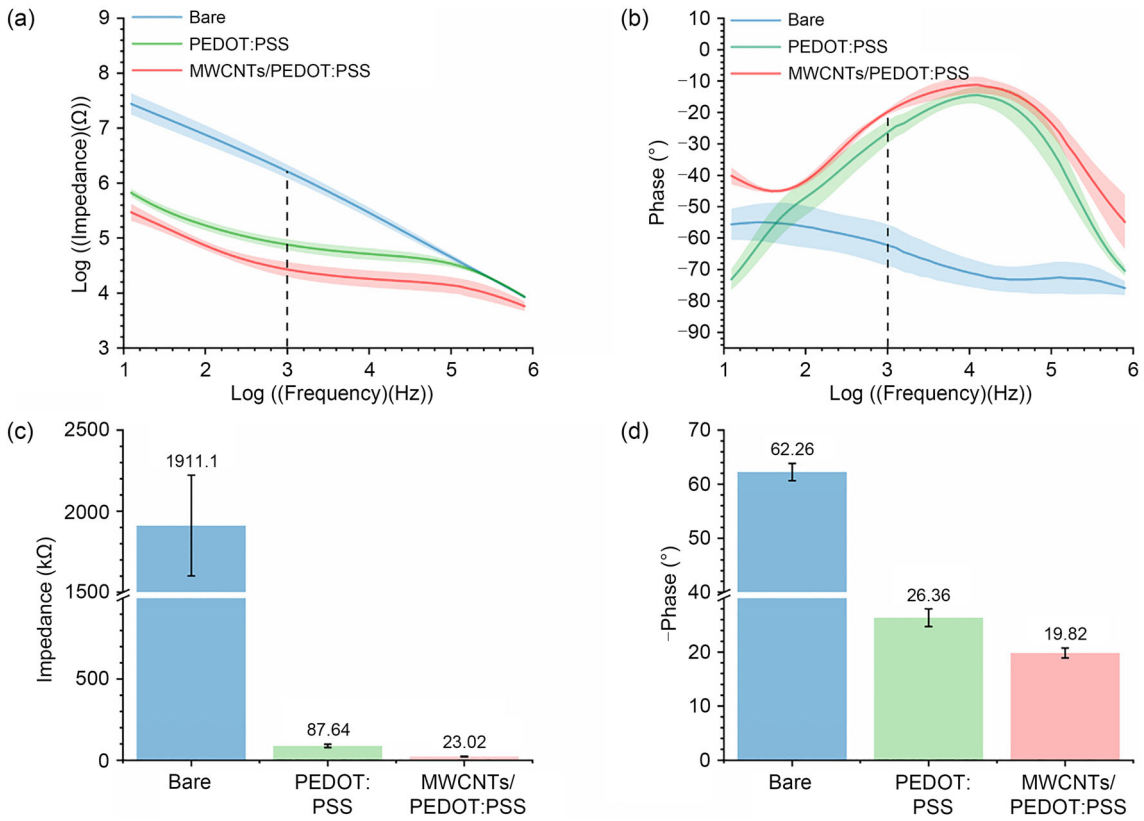

Fig. 3 Electrical characterization of the bare MEA, PEDOT:PSS-modified MEA, and MWCNTs/PEDOT:PSS-modified MEA. **a** Impedance characteristics of microelectrodes at different frequencies. **b** Phase characteristics of microelectrodes at different frequencies. **c** The average impedance value of microelectrodes at 1 kHz. **d** The average phase value of microelectrodes at 1 kHz. Data are presented as mean±standard error (n=10). MEA: microelectrode array; PEDOT: poly(3,4-ethylenedioxythiophene); PSS: poly(styrene sulfonate); MWCNTs: multiwalled carbon nanotubes

repeated-measure analysis of variance (ANOVA) was used. Significance is indicated by $^{*}p<0.05$, $^{**}p<0.01$, $^{***}p<0.001$, and $^{****}p<0.0001$.

Results

Characterization of the morphological and electrical properties of the MEA

Figure 2j shows that the surface of the MEA modified with MWCNTs/PEDOT:PSS remained dark. Moreover, scanning electron microscopy (SEM) images show that the MWCNTs/PEDOT:PSS modification provided the MEA with a rougher and more porous surface (Figs. 2k and 2l). Porous materials can increase electrode surface area, thereby promoting cell adhesion and neurite outgrowth.

As shown in Figs. 3a and 3b, the electrical characteristics of bare microelectrodes and microelectrodes modified using different materials were compared using electrochemical impedance spectroscopy at a scan range of 10–1×10^6 Hz. Figure 3c shows that the mean impedance of electrodes at a frequency of 1 kHz changed from (1911.1±310.7) kΩ (bare) to (87.64±9.7) kΩ (PEDOT:PSS) and (23.02±2.5) kΩ (MWCNTs/PEDOT:PSS). Figure 3d shows that the mean phase of the electrodes at 1 kHz frequency increased from −62.26°±1.6° (bare) to −26.36°±1.64° (PEDOT:PSS) and −19.82°±0.92° (MWCNTs/PEDOT:PSS). Taken together, these results illustrate that the modification of MWCNTs/PEDOT:PSS enhanced the detection and recording properties of the MEA.

To demonstrate the stability and efficacy of MWCNTs/PEDOT:PSS for acute experiments, we mimicked electrode implantation into the brain to test whether the electrode material would fall off. We used agarose gel to mimic the consistency of the brain material and implanted an electrode into the gel at a speed of 1 μm/s. The electrode was kept there for 1 h and then removed. By comparing the electrode before and after implantation, we found that the modified material was securely attached to the electrode (Fig. S4 in Supplementary Information). We therefore concluded that this material has excellent stability during acute experiments.

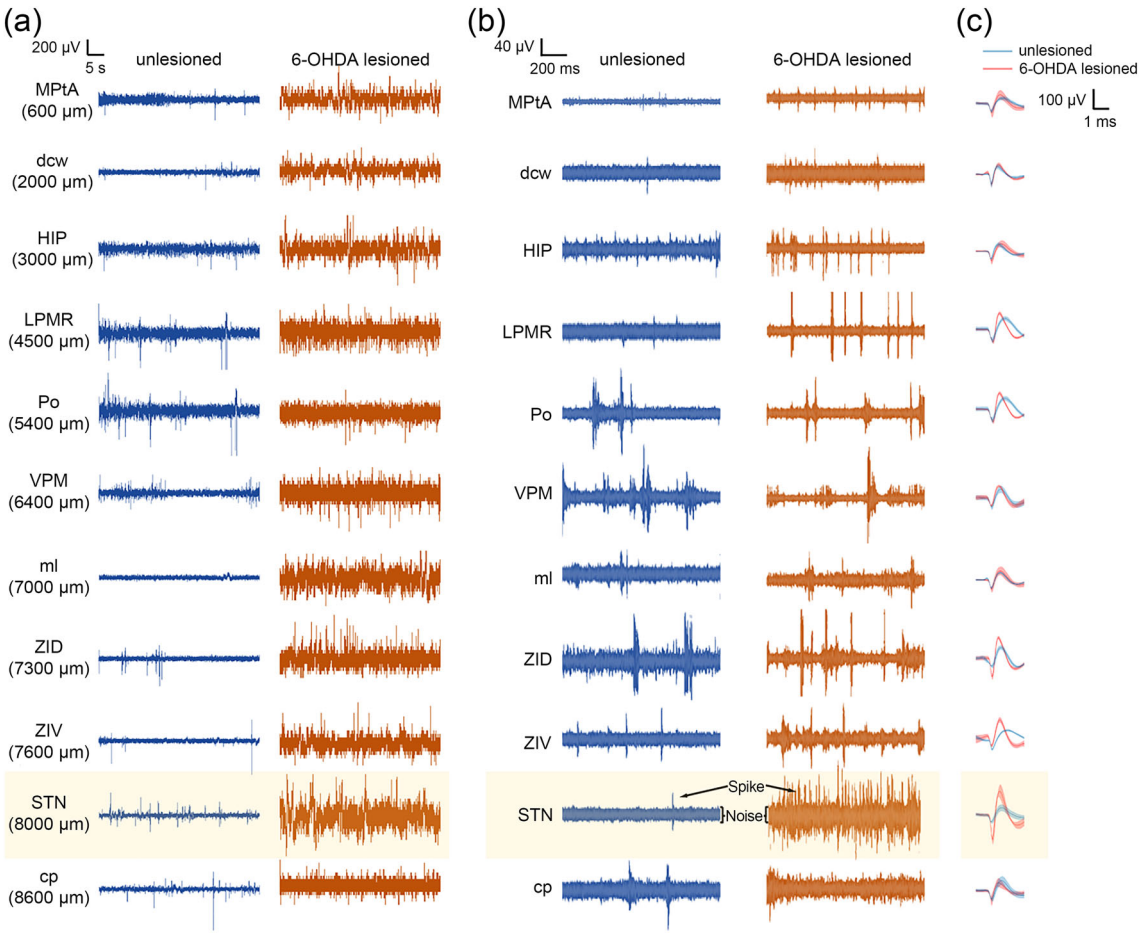

Fig. 4 LFP signal and spike activity mapping at different depths of the bilateral brain of PD rats (n=3). **a** LFP variation in the unlesioned side of the rat brain from the MPtA to the cp at eleven typical locations (left) and LFP variation in the 6-OHDA lesioned side of the rat brain at the corresponding depth (right). **b** Neural spike firing variation from the MPtA to the cp at eleven typical locations in the unlesioned side (left) and the 6-OHDA lesioned side (right) of rat brains. **c** Mean spike pattern of the 6-OHDA lesioned and unlesioned sides of rat brains from the MPtA to the cp at eleven typical locations. LFP: local field potential; PD: Parkinson's disease; MPtA: medial parietal association cortex; dcw: deep cerebral white matter; HIP: hippocampus; LPMR: lateral posterior thalamic nucleus, mediorostral part; Po: the post thalamic nuclear group; VPM: the ventral posteromedial thalamic nucleus; ml: medial lemniscus; ZID: the dorsal part of the zona incerta; ZIV: the ventral part of the zona incerta; STN: subthalamic nucleus; cp: cerebral peduncle; 6-OHDA: 6-hydroxydopamine hydrobromide

Mapping of cellular level neural signals in the bilateral brain

We then compared the PD STN and normal STN using electrophysiological signals recorded by the fabricated MEA from MPtA (600 μm) to the cp (8600 μm) areas of the bilateral brains of PD rats. As shown in Figs. 4a and 4b, variations in neural LFPs and spikes from the MPtA to the cp were found between 6-OHDA-lesioned and unlesioned brains. Mean spike waveforms are shown in Fig. 4c. Compared with nuclei from unlesioned brains, LFPs fluctuated more dramatically, and the spike firing mode was denser and more intense in the 6-OHDA-lesioned brain. These results demonstrated that the MEA could detect neural information in real time and identify nuclei by differences in firing mode.

The LFP power, spike firing rate, and spike amplitude of each nucleus in the bilateral brain implantation pathway (i.e., from MPtA to cp) were then compared statistically. Compared to the unlesioned brain, the nucleus of 6-OHDA-lesioned brains showed a higher LFP power value at 0–100 Hz (Fig. 5a). Moreover, the spike firing rate of the 6-OHDA-lesioned brain was higher than that of the unlesioned brain (Fig. 5b). Figure 5c shows a comparison of spike amplitude between the 6-OHDA-lesioned and unlesioned brains. These results illustrated that the neural activity of the 6-OHDA-lesioned brain exhibited higher amplitude than the unlesioned brain. Dopaminergic depletion in the 6-OHDA-lesioned brain can cause alterations in neuronal firing patterns in related nuclei, and may account for the hyperexcitability of neuronal firing in the 6-OHDA-lesioned brain compared to

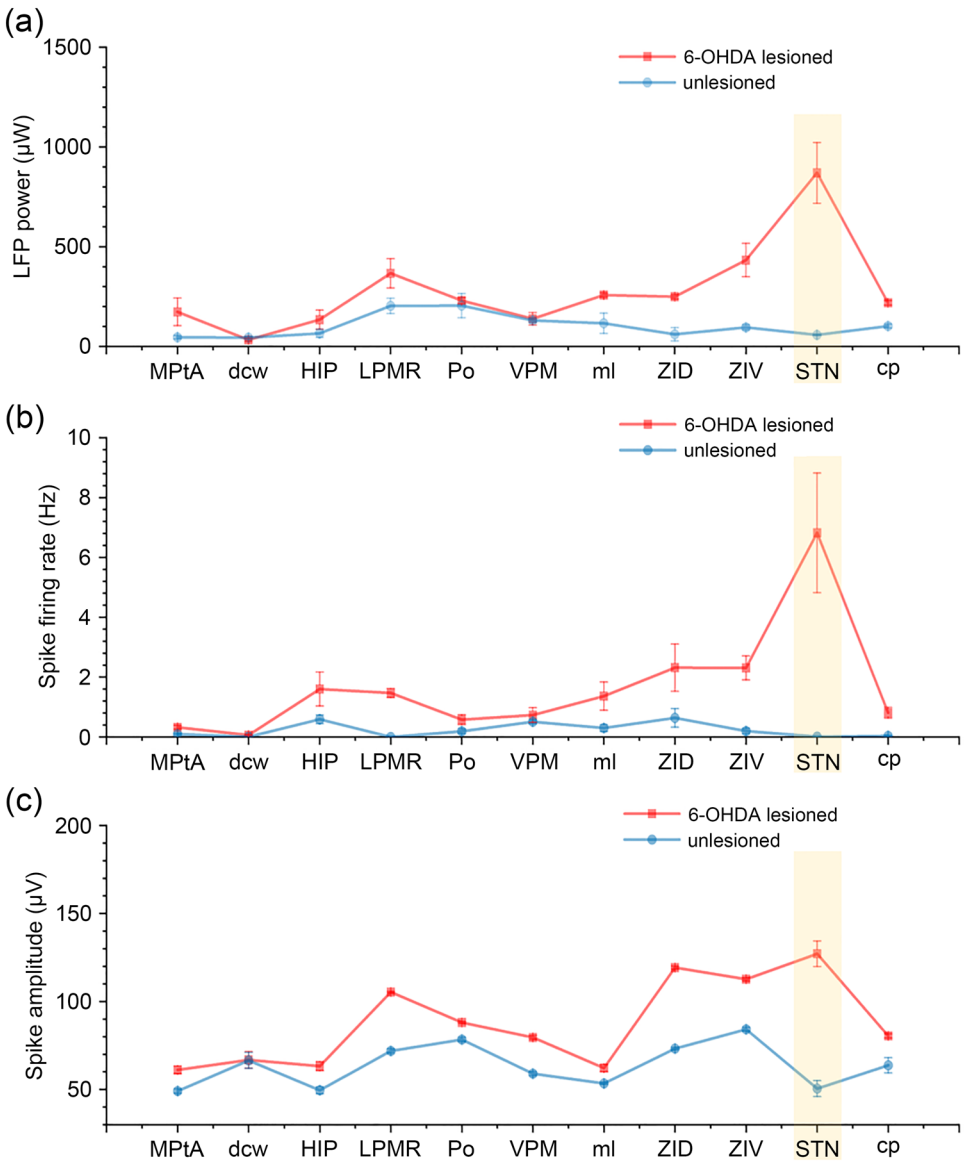

Fig. 5 Mean neural activity at different depths of the bilateral brain of PD rats (n=3). **a** Mean variation in total LFP (0–100 Hz) power from the MPtA to the cp in the 6-OHDA lesioned and unlesioned sides of rat brains. **b** Mean variation in the neural spike firing rate from the MPtA to the cp of the 6-OHDA lesioned and unlesioned sides of rat brains. **c** Mean variation in neural spike amplitude from the MPtA to the cp in the 6-OHDA lesioned and unlesioned sides of rat brains. PD: Parkinson's disease; LFP: local field potential; 6-OHDA: 6-hydroxydopamine hydrobromide; MPtA: medial parietal association cortex; dcw: deep cerebral white matter; HIP: hippocampus; LPMR: lateral posterior thalamic nucleus, mediorostral part; Po: the post thalamic nuclear group; VPM: the ventral posteromedial thalamic nucleus; ml: medial lemniscus; ZID: the dorsal part of the zona incerta; ZIV: the ventral part of the zona incerta; STN: subthalamic nucleus; cp: cerebral peduncle

the unlesioned control [35]. Overall, these results showed that during the implantation process, the neural signals detected in the unlesioned brain by MEAs were relatively infrequent, and the neural signals detected in the 6-OHDA-lesioned brain by MEAs were much more intense.

Precise localization of the STN using neural spikes and LFPs

Figures 6a and 6b show a diagram of the MEA entering the upper boundary of the STN and exiting its lower boundary. Also shown are typical neural signals from the 6-OHDA-lesioned rat brain. Notably, the MEA simultaneously acquired neural signals from the STN and its upper boundary nucleus (ZIV) when the MEA entered the STN, and simultaneously acquired neural signals from the STN and its lower boundary nucleus (cp) when the MEA exited the STN. Overall, the raw spike discharge mode in the STN was much more intense than that in the ZIV or cp nuclei.

The typical spike firing mode and LFP waveform of the STN and its surrounding nuclei in the 6-OHDA-lesioned brain are shown in Fig. 6c. Waveforms of single-cell spikes recorded in the STN using different channels of the fabricated MEA are shown in Fig. S5 (Supplementary Information). Note that when the biosensor was implanted from the ZIV into the STN, we observed less background noise (Fig. 6a), rapid changes in spikes, which became intense and dense, and a higher frequency and amplitude of the LFP waveform. When the MEA passed through the STN, the spike firing rate, spike amplitude, and LFP waveform decreased.

Figure 6d shows the mean variations in electrophysiological signals above and below the STN in the 6-OHDA-lesioned

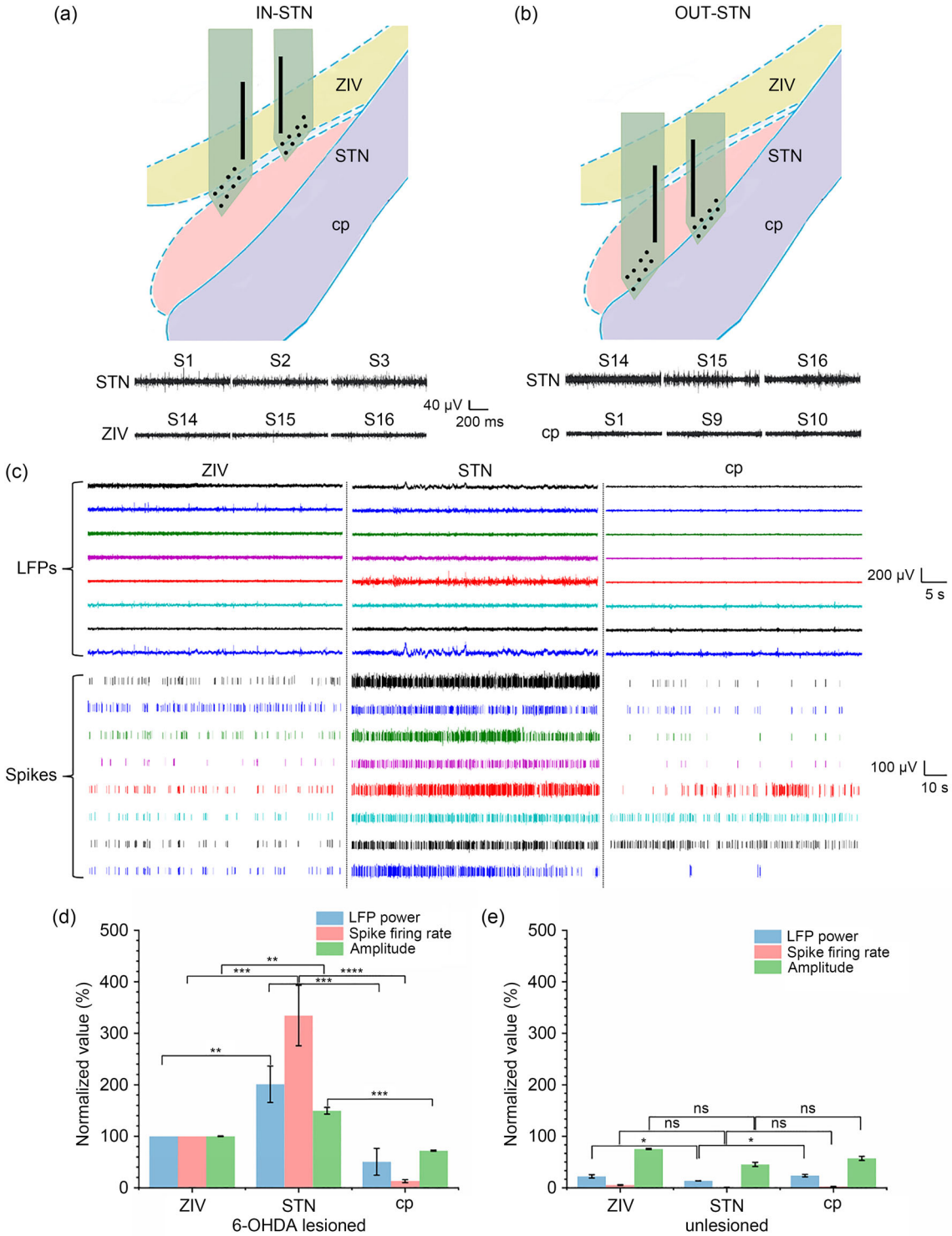

Fig. 6 Variation in neurophysiological signals from STN and related nuclei (i.e., ZIV and cp) in the bilateral brain of PD rats (n=3). **a** Schematic diagram of MEA trajectories positioned at the STN upper boundary and typical neuronal signals. **b** Schematic diagram of MEA trajectories positioned at the STN lower boundary and typical neuronal signals. **c** Raw LFPs and spikes from ZIV to cp as recorded by the MEA. **d** Normalized analysis of LFP power, spike firing rate, and spike amplitude at the ZIV, STN, and cp regions of the 6-OHDA lesioned side of PD rat brains. **e** Normalized analysis of LFP power, spike firing rate, and spike amplitude at the ZIV, STN, and cp regions of the unlesioned side of PD rat brains. Data are presented as mean±standard error, $^{*}p<0.05$, $^{**}p<0.01$, $^{***}p<0.001$, $^{****}p<0.0001$. STN: subthalamic nucleus; ZIV: the ventral part of the zona incerta; cp: cerebral peduncle; PD: Parkinson's disease; MEA: microelectrode array; LFP: local field potential; 6-OHDA: 6-hydroxydopamine hydrobromide; ns: not significant

brain. These were then compared to readings from the ZIV onward in the same 6-OHDA-lesioned brain. As MEAs were implanted more deeply, we observed an increase in average LFP power to (201±35)% (STN) and then a decrease to (51±26)% (cp). Over the same distance, the normalized spike firing rate increased from 100% (ZIV) to (334±59)% (STN) and decreased again to (13±3)% (cp). Furthermore, the normalized amplitude of this spike varied from 100% (ZIV) to (150±7)% (STN) to (72±1)% (cp). Compared with ZIV and cp, STN discharges are much more intense and show higher LFP power, a higher spike firing rate, and a higher spike amplitude. This may be related to the fact that abnormal neuronal activity in the STN is closely associated with motor impairments related to PD, while the correlation between ZIV and PD and that between cp and PD are relatively weak.

Figure 6e shows the mean variations in electrophysiological signals above and below the STN region of the unlesioned brain. These were compared to readings taken from the ZIV stage in the 6-OHDA-lesioned brain. The normalized LFP power was (22±3)% for ZIV, (13±1)% for STN, and (24±2)% for cp. The normalized spike firing rate decreased from (5±0.1)% (ZIV) to (1±0.1)% (STN) and increased to (3±0.1)% (cp). The normalized amplitude of the spike varied from (75±1)% (ZIV) to (45±4)% (STN) and (57±4)% (cp). In the unlesioned brain, we found no significant differences in the firing patterns of ZIV, STN, and cp. However, in these brain sections, neuronal firing was gentle compared to the corresponding nuclei on the lesioned side. The results demonstrated that neural spikes and LFPs showed similar trends following MEA implantation.

Identification and detection of the STN in the frequency domain

To better identify the STN, we further analyzed the power spectral density (PSD) of spikes and LFPs on transect from ZIV to cp in the 6-OHDA-lesioned brain. As shown in Fig. 7a, the peak PSD of LFPs in the ZIV was 3.77 μW in the delta band (0–4 Hz) at 1 Hz. For the STN, we observed the PSD of LFPs (Fig. 7b) as two bumps distributed in the delta and beta bands (i.e., 13–30 Hz). Furthermore, Fig. 7c shows that the PSD of LFPs in the cp was mainly located within the delta band. These results showed that compared to the ZIV and cp regions, the STN showed significant rhythmic oscillations in the beta band. For example, in the low-frequency band (0–30 Hz), the PSD of spikes showed similar curve peaks as was observed in the corresponding LFP power measurements from ZIV to cp (Figs. 7d–7f). Moreover, in the ZIV and cp, spike power was mainly located in the delta band, which is similar to the trend shown by the PSD of LFPs. However, in the STN, we observed that synchronous oscillations of the LFPs and spikes were located in the delta and beta frequency bands. Dyskinesia in Parkinsonian patients is thought to be correlated with beta oscillations in the STN [36, 37]. Thus, beta oscillations in the STN but not in the ZIV or cp may be related to the close association between the activity of the STN and PD-related motor impairments. This is consistent with previous findings, indicating that correlations between these impairments and the activity of the ZIV and cp are relatively weak.

Furthermore, this work compared the PSD of spikes and LFPs in the STN regions of 6-OHDA-lesioned and unlesioned brains. Peak spike power of the STN of the unlesioned brain was in the delta band, which was similar to the PSD of LFPs measured in the STN of the unlesioned brain (Fig. 7g). The PSDs of LFPs and spikes in the STN showed consistent difference between unlesioned and 6-OHDA-lesioned brains. Specifically, the PSDs of spikes and LFPs synchronously increased in the beta band and decreased in the delta band in the STN of the 6-OHDA-lesioned brain relative to the STN of the unlesioned brain. Moreover, LFP power decreased from (0.146±0.008) mW (in the unlesioned brain) to (0.10±0.008) mW (in the 6-OHDA-lesioned brain) in the delta band and increased from (0.005±0.001) mW (in the unlesioned brain) to (0.138±0.005) mW (in the 6-OHDA-lesioned brain) in the beta band (Fig. 7h). Previous research has mainly studied the beta oscillations associated with LFPs [38, 39], and here we observed that the spike and LFP PSDs both synchronously increased in the beta band of the STN, revealing the microscopic cause of beta oscillation in the STN. Furthermore, it has been established that delta waves correlate with sleep quality [40, 41]. Thus, variation in the PSD of LFPs and spikes in the delta band may contribute to sleep disorders in Parkinsonian patients.

Discussion

In this study, a fabricated MEA was proven to be able to realize the precise localization and detection of the STN using a rat model. Clinical localization of the STN is usually performed using a tungsten-tipped [42] or DBS electrode [10, 43]. To precisely and rapidly localize the STN, multiple neural probes may need to be implanted, which increases brain damage and decreases localization efficiency [42–44]. In contrast, the structural design of the 16-channel MEA reported here simultaneously obtained neural information in the STN without requiring multiple implantations. Moreover, the detection sites of the MEA were designed to track the shape of the STN, and this pattern of site deployment permits more efficient gathering of neural information on the cellular level to realize accurate and rapid localization of the STN. In addition, the use of MWCNTs/PEDOT:PSS makes the MEA surface rougher, thereby increasing the specific surface area of MEAs and permitting better adsorption of neurons, which in turn allows for even more accurate localization of the STN.

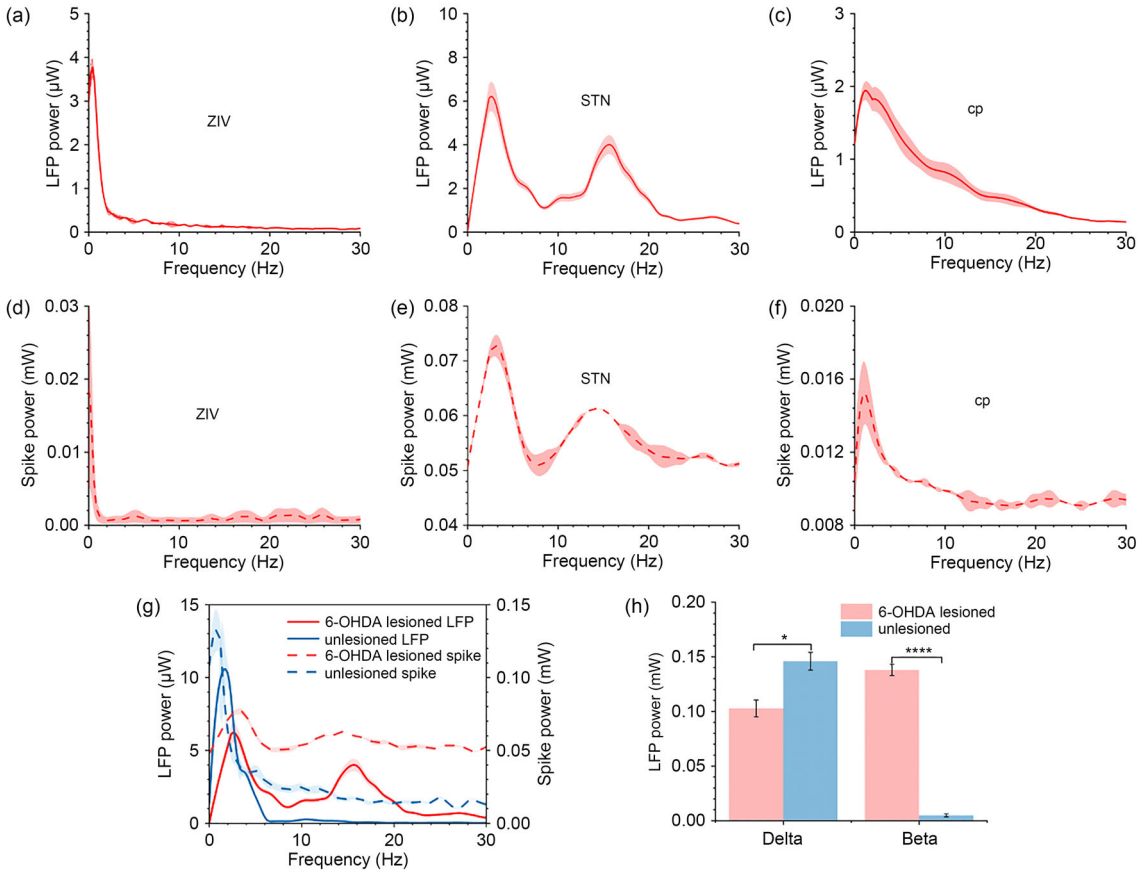

Fig. 7 Analysis of PSDs of spikes and LFPs. **a** PSD of LFPs in the ZIV (6-OHDA lesioned brain). **b** PSD of LFPs in the STN (6-OHDA lesioned brain) showing two bumps in the delta (0–4 Hz) and beta (13–30 Hz) bands. **c** PSD of LFPs in the cp (6-OHDA lesioned brain). **d** PSD of spikes in the ZIV (6-OHDA lesioned brain). **e** PSD of spikes in the STN (6-OHDA lesioned brain) showing two bumps in the delta and beta frequency bands. **f** PSD of spikes in the cp (6-OHDA lesioned brain). **g** PSD of spikes and LFPs in the STN of 6-OHDA lesioned and unlesioned brains, respectively. **h** Comparison of LFP power in the delta and beta frequency bands in the STN of 6-OHDA lesioned and unlesioned brains. Data are presented as mean±standard error, n=3, $^{*}p$<0.05, $^{****}p$<0.0001. PSD: power spectral density; LFPs: local field potentials; ZIV: the ventral part of the zona incerta; STN: subthalamic nucleus; cp: cerebral peduncle; 6-OHDA: 6-hydroxydopamine hydrobromide

In this work, the fabricated MEA was implanted into the bilateral brain of PD rats. Our results showed that, relative to unlesioned brains, 6-OHDA-lesioned brain measurements indicated denser spike firing and a more violent LFP waveform from the MPtA to cp. These effects may be caused by the abnormal discharge of nuclei due to dopamine depletion on the 6-OHDA-lesioned side. To recognize the boundaries of the STN in the 6-OHDA-lesioned brain, the detection sites of the MEAs were distributed at different depths so that the MEA device could simultaneously acquire neural signals from the STN as well as the upper and lower boundary nuclei of the STN. Next, we note that the observed firing mode in the STN was much more intense than in the ZIV or cp. To further analyze differences between the STN and upper and lower proximal nuclei, we provided an in-depth analysis of the spike and LFP activities of the ZIV, STN, and cp areas. We found that the STN discharges were much more intense and showed higher LFP power, spike firing rate, and spike amplitude. This may be related to the fact that abnormal neuronal activity in the STN has been shown to be closely associated with motor impairments in PD; in contrast, the activity of the ZIV and cp is less correlated with PD. Therefore, our results indicate that the MEAs can precisely and rapidly localize the STN.

Next, this work analyzed the PSD of spikes and LFPs in the ZIV, STN, and cp to use frequency data to identify the STN. Our results showed that spikes and LFPs were synchronized from the ZIV to cp (0–30 Hz). In the ZIV and cp, the spike power and LFP power were both located mainly in the delta band. However, in the STN, we observed two bumps of PSD for both the LFPs and spikes; these were located in the delta and beta frequency bands. This finding suggests that abnormal firing of the STN is associated with motor deficits in PD, while the ZIV and cp appear to have

little correlation with these motor symptoms. Compared to the STN of unlesioned brains, the LFP and spike power of the STN in 6-OHDA-lesioned brains decreased in the delta band and increased in the beta band, which is considered to be a cause of PD-related motor disorder. The delta band is correlated with sleep quality; thus, decreases in the LFP and spike power of the STN in the 6-OHDA-lesioned brain may cause sleep disorders for PD patients.

DBS of the STN has been shown to result in better treatment with fewer complications for PD patients [45, 46]. Precise localization of the STN is crucial for correct stimulation treatment and to avoid damaging surrounding nuclei. Here, the reported multichannel MEA achieved precise functional localization and detection of the STN in PD rats. Furthermore, this work provides a cellular-level marker for STN localization and generated data suggesting a relationship between STN activity and potential causes of sleep and movement disorders associated with PD. Overall, the proposed MEA provides a reliable tool for the precise localization and detection of deep brain nuclei.

Conclusions

In this paper, a novel deep brain implanted MEA was designed to follow the shape of the STN of rats to better detect and localize the STN. Furthermore, the detailed manufacturing process of this MEA is provided. Test results illustrated that the MEA detected neural information in real time and identified individual nuclei by differences in firing mode. Furthermore, the MEAs simultaneously acquired neural signals from the STN and nuclei along the upper or lower boundary of the STN. Moreover, we observed a higher spike firing rate, spike amplitude, local field potential power, and beta oscillations in the STN of 6-OHDA-lesioned brains, and these may therefore be biomarkers of STN localization. Compared with STN regions of unlesioned brains, we observed synchronized variation in the PSD of spikes and LFPs in the delta and beta bands in 6-OHDA-lesioned brains; these may be causes of sleep and motor disorders associated with PD. In conclusion, the proposed MEA can precisely localize deep brain nuclei, and our new findings may be useful for the development of novel treatments of PD.

Supplementary Information The online version contains supplementary material available at https://doi.org/10.1007/s42242-023-00266-y.

Acknowledgements This research was funded by the National Natural Science Foundation of China (Nos. L2224042, T2293731, 62121003, 61960206012, 61973292, 62171434, 61975206, and 61971400), the Frontier Interdisciplinary Project of the Chinese Academy of Sciences (No. XK2022XXC003), the National Key Research and Development Program of China (Nos. 2022YFC2402501 and 2022YFB3205602), the Major Program of Scientific and Technical Innovation 2030 (No. 2021ZD02016030), and the Scientific Instrument Developing Project of the Chinese Academy of Sciences (No. GJJSTD20210004). The authors thank Yilin Song for her advice on grammar revisions and polishing.

Author contributions LYJ was involved in conceptualization, methodology, visualization, investigation, and writing—original draft preparation, review & editing, and supervision. ZJX was involved in investigation and data curation. PHF, BTL, WX, and FM were involved in methodology. RLH, JS, QLJ, YXZ, and YMD were involved in formal analysis. MXW, YRW, and XXC were involved in project administration and writing—review & editing, and checked it for final submission. All authors have approved the submitted version.

Declarations

Conflict of interest The authors declare that they have no conflict of interest.

Ethical approval All institutional and national guidelines for the care and use of laboratory animals were followed. All experiments were performed with the permission of the Beijing Association on Laboratory Animal Care under license number SYXK(JING)2020-0045.

Data availability All data needed to support the conclusions in the paper are provided in the paper and the supplementary materials.

References

1. Schmauss M (2022) Depression and Parkinson's disease. Fortschritte Der Neurol Psychiatr 90(04):145–146. https://doi.org/10.1055/a-1683-1840
2. Ceballos-Baumann A (2022) Parkinson's disease—what is new? Dtsch Med Wochenschr 147(06):337–343. https://doi.org/10.1055/a-1646-6321
3. Guatteo E, Yee A, McKearney J et al (2013) Dual effects of L-DOPA on nigral dopaminergic neurons. Exp Neurol 247:582–594. https://doi.org/10.1016/j.expneurol.2013.02.009
4. Zhao YT, Liu L, Zhao Y et al (2022) The effect and safety of levodopa alone versus levodopa sparing therapy for early Parkinson's disease: a systematic review and meta-analysis. J Neurol 269(4):1834–1850. https://doi.org/10.1007/s00415-021-10830-0
5. Jahanshahi M, Leimbach F, Rawji V (2022) Short and long-term cognitive effects of subthalamic deep brain stimulation in Parkinson's disease and identification of relevant factors. J Parkinsons Dis 12(7):2191–2209. https://doi.org/10.3233/jpd-223446
6. Herzog J, Fietzek U, Hamel W et al (2004) Most effective stimulation site in subthalamic deep brain stimulation for Parkinson's disease. Mov Disord 19(9):1050–1054. https://doi.org/10.1002/mds.20056
7. Kinfe TM, Vesper J (2013) The impact of multichannel microelectrode recording (MER) in deep brain stimulation of the basal ganglia. Acta Neurochir Suppl 117:27–33. https://doi.org/10.1007/978-3-7091-1482-7_5
8. Richardson RM, Ostrem JL, Starr PA (2009) Surgical repositioning of misplaced subthalamic electrodes in Parkinson's disease: location of effective and ineffective leads. Stereotact Funct Neurosurg 87(5):297–303. https://doi.org/10.1159/000230692
9. Cui ZQ, Pan LS, Song HF et al (2016) Intraoperative MRI for optimizing electrode placement for deep brain stimulation of the subthalamic nucleus in Parkinson disease. J Neurosur 124(1):62–69. https://doi.org/10.3171/2015.1.Jns141534

10. Horn A, Li NF, Dembek TA et al (2019) Lead-DBS v2: towards a comprehensive pipeline for deep brain stimulation imaging. Neuroimage 184:293–316. https://doi.org/10.1016/j.neuroimage.2018.08.068
11. Novak P, Przybyszewski AW, Barborica A et al (2011) Localization of the subthalamic nucleus in Parkinson disease using multiunit activity. J Neurol Sci 310(1–2):44–49. https://doi.org/10.1016/j.jns.2011.07.027
12. Sterio D, Zonenshayn M, Mogilner AY et al (2002) Neurophysiological refinement of subthalamic nucleus targeting. Neurosurgery 50(1):58–67. https://doi.org/10.1097/00006123-200201000-00012
13. Benabid AL, Pollak P, Gross C et al (1993) Acute and long-term effects of subthalamic nucleus stimulation in Parkinson's disease. Stereotact Funct Neurosurg 62(1–4):76–84. https://doi.org/10.1159/000098600
14. Limousin P, Pollak P, Benazzouz A et al (1995) Effect on Parkinsonian signs and symptoms of bilateral subthalamic nucleus stimulation. Lancet 345(8942):91–95. https://doi.org/10.1016/s0140-6736(95)90062-4
15. Gross RE, Krack P, Rodriguez-Oroz MC et al (2006) Electrophysiological mapping for the implantation of deep brain stimulators for Parkinson's disease and tremor. Mov Disord 21(S14):S259–S283. https://doi.org/10.1002/mds.20960
16. Ozturk M, Kaku H, Jimenez-Shahed J et al (2020) Subthalamic single cell and oscillatory neural dynamics of a dyskinetic medicated patient with Parkinson's disease. Front Neurosci 14:391. https://doi.org/10.3389/fnins.2020.00391
17. Tamir I, Wang D, Chen W et al (2020) Eight cylindrical contact lead recordings in the subthalamic region localize beta oscillations source to the dorsal STN. Neurobiol Dis 146:105090. https://doi.org/10.1016/j.nbd.2020.105090
18. Mo F, Xu ZJ, Yang GC et al (2022) Single-neuron detection of place cells remapping in short-term memory using motion microelectrode arrays. Biosens Bioelectron 217:114726. https://doi.org/10.1016/j.bios.2022.114726
19. Buzsaki G, Anastassiou CA, Koch C (2012) The origin of extracellular fields and currents—EEG, ECoG LFP and spikes. Nat Rev Neurosci 13(6):407–420. https://doi.org/10.1038/nrn3241
20. Buzsaki G (2012) How do neurons sense a spike burst? Neuron 73(5):857–859. https://doi.org/10.1016/j.neuron.2012.02.013
21. Xiao GH, Song YL, Zhang Y et al (2019) Microelectrode arrays modified with nanocomposites for monitoring dopamine and spike firings under deep brain stimulation in rat models of Parkinson's disease. ACS Sens 4(8):1992–2000. https://doi.org/10.1021/acssensors.9b00182
22. Zhang Y, Xu SW, Xiao GH et al (2019) High frequency stimulation of subthalamic nucleus synchronously modulates primary motor cortex and caudate putamen based on dopamine concentration and electrophysiology activities using microelectrode arrays in Parkinson's disease rats. Sens Actuat B Chem 301:127126. https://doi.org/10.1016/j.snb.2019.127126
23. Prajapati DG, Kandasubramanian B (2019) Progress in the development of intrinsically conducting polymer composites as biosensors. Macromol Chem Phys 220(10):26. https://doi.org/10.1002/macp.201800561
24. Wang XJ, Sjoberg-Eerola P, Eriksson JE et al (2010) The effect of counter ions and substrate material on the growth and morphology of poly(3,4-ethylenedioxythiophene) films: towards the application of enzyme electrode construction in biofuel cells. Synth Met 160(13–14):1373–1381. https://doi.org/10.1016/j.synthmet.2010.01.033
25. King ZA, Shaw CM, Spanninga SA et al (2011) Structural, chemical and electrochemical characterization of poly(3,4-ethylenedioxythiophene) (PEDOT) prepared with various counterions and heat treatments. Polymer 52(5):1302–1308. https://doi.org/10.1016/j.polymer.2011.01.042
26. Ludwig KA, Uram JD, Yang JY et al (2006) Chronic neural recordings using silicon microelectrode arrays electrochemically deposited with a poly(3,4-ethylenedioxythiophene) (PEDOT) film. J Neural Eng 3(1):59–70. https://doi.org/10.1088/1741-2560/3/1/007
27. Furukawa Y, Shimada A, Kato K et al (1830) (2013) Monitoring neural stem cell differentiation using PEDOT-PSS based MEA. Biochim Biophys Acta-Gen Subj 9:4329–4333. https://doi.org/10.1016/j.bbagen.2013.01.022
28. Groenendaal L, Jonas F, Freitag D et al (2000) Poly(3,4-ethylenedioxythiophene) and its derivatives: past, present, and future. Adv Mater 12(7):481–494. https://doi.org/10.1002/(SICI)1521-4095(200004)12:7%3c481::AID-ADMA481%3e3.0.CO;2-C
29. Li XR, Song YL, Xiao GH et al (2021) PDMS-parylene hybrid, flexible micro-ECoG electrode array for spatiotemporal mapping of epileptic electrophysiological activity from multicortical brain regions. ACS Appl Bio Mater 4(11):8013–8022. https://doi.org/10.1021/acsabm.1c00923
30. Zhou HH, Cheng X, Rao L et al (2013) Poly(3,4-ethylenedioxythiophene)/multiwall carbon nanotube composite coatings for improving the stability of microelectrodes in neural prostheses applications. Acta Biomater 9(5):6439–6449. https://doi.org/10.1016/j.actbio.2013.01.042
31. Keefer EW, Botterman BR, Romero MI et al (2008) Carbon nanotube coating improves neuronal recordings. Nat Nanotechnol 3(7):434–439. https://doi.org/10.1038/nnano.2008.174
32. Malarkey EB, Parpura V (2010) Carbon nanotubes in neuroscience. In: Czernicki Z, Baethmann A, Ito U et al (Eds.), Brain Edema XIV: Acta Neurochirurgica Supplementum. Springer, Vienna, p.337–341
33. He EH, Xu SW, Xiao GH et al (2021) MWCNTs/PEDOT:PSS nanocomposites-modified microelectrode array for spatial dynamics recording of epileptic discharges in multi-subregion of hippocampal slice. Sens Actuat B Chem 329:129190. https://doi.org/10.1016/j.snb.2020.129190
34. Xu SW, Zhang Y, Zhang S et al (2018) An integrated system for synchronous detection of neuron spikes and dopamine activities in the striatum of Parkinson monkey brain. J Neurosci Method 304:83–91. https://doi.org/10.1016/j.jneumeth.2018.04.015
35. McGregor MM, Nelson AB (2019) Circuit mechanisms of Parkinson's disease. Neuron 101(6):1042–1056. https://doi.org/10.1016/j.neuron.2019.03.004
36. Sharott A, Gulberti A, Hamel W et al (2018) Spatio-temporal dynamics of cortical drive to human subthalamic nucleus neurons in Parkinson's disease. Neurobiol Dis 112:49–62. https://doi.org/10.1016/j.nbd.2018.01.001
37. Asadi A, Asl MM, Vahabie AH et al (2022) The origin of abnormal beta oscillations in the Parkinsonian corticobasal ganglia circuits. Parkinsons Dis 2022:13. https://doi.org/10.1155/2022/7524066
38. Li YJ, Zeng YQ, Lin MG et al (2023) Beta oscillations of dorsal STN as a potential biomarker in Parkinson's disease motor subtypes: an exploratory study. Brain Sci 13(5):737. https://doi.org/10.3390/brainsci13050737
39. Weinberger M, Mahant N, Hutchison WD et al (2006) Beta oscillatory activity in the subthalamic nucleus and its relation to dopaminergic response in Parkinson's disease. J Neurophysiol 96(6):3248–3256. https://doi.org/10.1152/jn.00697.2006
40. Thompson JA, Tekriwal A, Felsen G et al (2018) Sleep patterns in Parkinson's disease: direct recordings from the subthalamic

nucleus. J Neurol Neurosurg Psychiatry 89(1):95–104. https://doi.org/10.1136/jnnp-2017-316115
41. Kayaba M, Park I, Iwayama K et al (2017) Energy metabolism differs between sleep stages and begins to increase prior to awakening. Metab-Clin Exp 69:14–23. https://doi.org/10.1016/j.metabol.2016.12.016
42. Marmor O, Valsky D, Joshua M et al (2017) Local versus volume conductance activity of field potentials in the human subthalamic nucleus. J Neurophysiol 117(6):2140–2151. https://doi.org/10.1152/jn.00756.2016
43. Horn A, Kuhn AA (2015) Lead-DBS: a toolbox for deep brain stimulation electrode localizations and visualizations. Neuroimage 107:127–135. https://doi.org/10.1016/j.neuroimage.2014.12.002
44. Steigerwald F, Potter M, Herzog J et al (2008) Neuronal activity of the human subthalamic nucleus in the Parkinsonian and nonparkinsonian state. J Neurophysiol 100(5):2515–2524. https://doi.org/10.1152/jn.90574.2008
45. Benabid AL, Chabardes S, Mitrofanis J et al (2009) Deep brain stimulation of the subthalamic nucleus for the treatment of Parkinson's disease. Lancet Neurol 8(1):67–81. https://doi.org/10.1016/s1474-4422(08)70291-6
46. Rosin B, Slovik M, Mitelman R et al (2011) Closed-loop deep brain stimulation is superior in ameliorating Parkinsonism. Neuron 72(2):370–384. https://doi.org/10.1016/j.neuron.2011.08.023